Laminar-Turbulent Transition behind Discrete Roughness Elements in a High-Speed Boundary Layer

Meelan Choudhari[†], Fei Li[*], Minwei Wu[**], Chau-Lyan Chang[*],
Computational AeroSciences Branch, NASA Langley Research Center, Hampton, VA 23681

Jack Edwards[‡],
North Carolina State University, Raleigh, NC 27695

Michael Kegerise[***], and Rudolph King[***]
Flow Physics and Control Branch, NASA Langley Research Center, Hampton, VA 23681

Computations are performed to study the flow past an isolated roughness element in a Mach 3.5, laminar, flat plate boundary layer. To determine the effects of the roughness element on the location of laminar-turbulent transition inside the boundary layer, the instability characteristics of the stationary wake behind the roughness element are investigated over a range of roughness heights. The wake flow adjacent to the spanwise plane of symmetry is characterized by a narrow region of increased boundary layer thickness. Beyond the near wake region, the centerline streak is surrounded by a pair of high-speed streaks with reduced boundary layer thickness and a secondary, outer pair of lower-speed streaks. Similar to the spanwise periodic pattern of streaks behind an array of regularly spaced roughness elements, the above wake structure persists over large distances and can sustain strong enough convective instabilities to cause an earlier onset of transition when the roughness height is sufficiently large. Time accurate computations are performed to clarify additional issues such as the role of the nearfield of the roughness element during the generation of streak instabilities, as well as to reveal selected details of their nonlinear evolution. Effects of roughness element shape on the streak amplitudes and the interactions between multiple roughness elements aligned along the flow direction are also investigated.

Nomenclature

A_u	=	streak amplitude based on one half of maximum spanwise variation in streamwise velocity
b	=	width of each vertical face of the diamond trip
h	=	trip height
M	=	Mach number
M_e	=	Mach number near boundary layer edge
Re_θ	=	Reynolds number based on momentum thickness
Re_{kk}	=	Reynolds number based on roughness height and flow conditions at this height within the incoming boundary layer
w	=	frontal half width of trip
(x,y,z)	=	streamwise, wall-normal, and spanwise coordinates, respectively
$\delta_{0.995}$	=	Boundary layer thickness based on $u/U_\infty = 0.995$
ν_∞	=	kinematic viscosity at free-stream conditions

[†] Aerospace Technologist, M.S. 128. Associate Fellow, AIAA.
* Aerospace Technologist, M.S. 128.
** Research Scientist, National Institute of Aerospace, Hampton, VA. Member, AIAA.
[‡] Professor, Department of Mechanical and Aerospace Engineering. Associate Fellow, AIAA.
*** Aerospace Technologist, M.S. 170.

I. INTRODUCTION

Surface roughness is known to have a substantial impact on the aerothermodynamic predictions for a hypersonic vehicle, regardless of the state of the boundary layer. When the incoming boundary-layer flow is laminar, the presence of 3D surface roughness tends to accelerate the laminar-turbulent transition process, which can result in a dramatic increase in both drag and aerodynamic heating of the vehicle. In scramjet applications, artificial roughness elements are often employed for intentional tripping of the boundary layer on the forebody of the vehicle in order to prevent engine unstart and to minimize the flow non-uniformities at the entrance to the combustor inlet.

Three-dimensional surface roughness may occur as discrete, isolated roughness elements (e.g., protruding gap fillers or cavities due to impact damage over the shuttle orbiter surface) or as a denser, non-localized (i.e., distributed) roughness such as that over an ablated surface. There are multiple ways in which a discrete 3D roughness element could influence the laminar-turbulent transition in a hypersonic boundary layer, depending on the size and shape of the roughness element. Empirical observations[1,2] suggest that when the roughness height exceeds a critical value the transition front begins to move upstream relative to that over a smooth surface in the same disturbance environment. As the height parameter is increased beyond this critical value, the transition location continues to shift upstream until it asymptotes to a location in the near wake of the roughness element (or, in certain cases, a finite distance downstream of the roughness element[2]) for roughness heights larger than what is known as the effective trip height. Both the critical and effective values of the height parameter are influenced by the shape of the roughness element and the external disturbance environment.[2]

Despite the common presence of surface roughness and its impact on the design and operation of hypersonic vehicles, the physical mechanisms underlying the phenomenon of roughness-induced transition are far from being understood at this time[1–8]. The correlation[9] between roughness-induced subcritical transition on blunt nose tips and the optimal, non-modal amplification factors associated with the (unperturbed) boundary-layer flow provides indirect evidence to support the role of transient growth in the context of transition due to distributed surface roughness. However, additional work is necessary to establish the physical validity of this correlation. Furthermore, the measurement database pertaining to known roughness shapes in a flight (or flight relevant) disturbance environment is severely limited. To help rectify these deficiencies, an intensive research efforts has been initiated under NASA's Fundamental Aeronautics Program (Hypersonics Project), Space Exploration Program, and by the United States Air Force. This broad set of efforts encompasses wind tunnel experiments in conventional[10] and quiet flow facilities,[2,11] flight experiments,[12–16] and fundamental computational activities.[17–20]

Ref. 17 investigated the flow behind an array of ramp and diamond trips in the context of a 1:3 scale model of the forebody of the Hyper-X vehicle.[8] The flow in the wake of the trip array mounted on the first compression ramp of the forebody was shown to support multiple modes of convective instabilities and the growth of the instabilities was strong enough to cause transition onset before the end of the first ramp as measured during an earlier set of wind tunnel experiments. The flow behind an isolated roughness element was modeled in Ref. 18, which addressed the potential onset of spontaneous unsteadiness behind the roughness element. It was shown that the wake flow became increasingly resistant to vortex shedding at supersonic Mach numbers, with the computations indicating a steady wake flow to be a realizable solution at values of the roughness height Reynolds number that would have resulted in strong vortex shedding at low Mach numbers. The transition mechanisms associated with the stationary wake flow behind an isolated roughness element are investigated in the present paper. Due to space limitations, attention is confined to the overall flow-field behavior and major parameter trends. An in-depth description of the flow field details based on the computational dataset is deferred to a future report.

II. FLOW CONDITIONS AND TRIP GEOMETRY

The present computations model a Mach 3.5 flow configuration that is relevant to an upcoming experiment in NASA Langley's Supersonic Low Disturbance Tunnel. [11] The in-depth measurements to be acquired during this experiment will help validate computational predictions related to transition mechanisms underlying roughness induced tripping, as well as to help delineate the limitations of the theoretical methodology presented herein and/or help improve the reliability of the predictions based on this methodology. Based on the design of this experiment, a diamond shaped trip (i.e., a square prism inclined at 45 degrees to the incoming free stream, Fig. 1) is placed approximately 1.625" downstream from the sharp leading edge of a 16" long flat plate model. The baseline width of each vertical face of the diamond trip is given by b = 0.050", while the trip height h is varied over a wide range up to 0.025". The stagnation pressure is equal to 25 psi, so that the thickness of the unperturbed boundary layer at the roughness location is approximately $\delta_{0.995} = 0.027$", with a Reynolds number of $U_\infty \delta_{0.995}/\nu_\infty \approx 6750$. The Reynolds number Re_{kk} based on the baseline trip height of h = 0.015" and the flow conditions at this height corresponds to $Re_{kk} \approx 547$. With Re_θ/M_e at the roughness location being equal to 118.6, the correlation parameter $Re_\theta/M_e\ k/\delta_{0.995}$ from Ref. 7 equals approximately 66 for $k \equiv h = 0.015$". Based on linear stability predictions, smooth surface transition due to first mode instability is not expected to occur until $x = 40$", i.e., well beyond the 16-inch length of this plate. Here, we assume the flat plate to be aligned with the y=0 plane and the incoming free-stream flow to be along the x axis, so that coordinates axes y and z are along the wall-normal and spanwise directions, respectively.

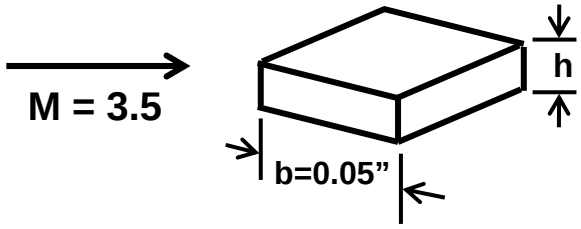

Figure 1. Schematic of diamond trip.

III. ISOLATED DIAMOND TRIP IN SUPERSONIC LOW DISTURBANCE TUNNEL (SLDT)

To obtain the mean-flow solution in the presence of the trip array, the compressible Navier-Stokes equations are solved using local time stepping in conjunction with an implicit technique. The Piecewise Parabolic Method[21] is used to extend the first-order low diffusion flux splitting scheme (LDFSS) upwind scheme to 4th order for advection terms in smooth regions of the flow. The immersed boundary (IB) technique as implemented by Choi et al.[22] and Ghosh et al.[23] is used to simulate the effects of the trip element on the surrounding flow.

The computations are limited to a narrow spanwise region centered on the trip element, and any large-scale 3D effects associated with the finite-span model are neglected in this study. For simplicity, the inflow conditions are defined via the self-similar solution to the boundary-layer equations at the free-stream conditions of interest. The number of grid points in streamwise, wall-normal, and spanwise grid points is 1281, 289, and 45, respectively, so that the total number of cells within the 3D immersed boundary mesh over one half of the spanwise region is approximately 16 million. The grid count as well as the relative grid distribution was based on previous computations for a spanwise periodic array of trip elements[17] as well as test calculations for the baseline configuration of h = 0.015". As noted subsequently, the flow fields for the periodic and isolated roughness configurations are quite similar. A grid convergence study for the flow past the periodic array of trip elements using the same code was

already performed during the earlier effort.[17] However, additional computations were performed for the h = 0.015" roughness element using a grid with 46 million cells (referred to herein as the "finer grid") that was obtained by increasing the grid density by approximately 40 percent in each coordinate direction. It should be noted that an IB technique may not be ideal for capturing the details in the immediate vicinity of the roughness element; however, previous computations for a ramp trip configuration[17] have shown satisfactory overall agreement between the predictions of the wake flow characteristics derived from the IB methodology and a conventional body-fitted grid.

Typically, the base flow computations were continued for at least 10,000 iterations after the residual convergence stagnated around $O(10^{-12})$, to ensure that any locally separated regions were no longer evolving in the eyeball norm.

A. Mean Flow-Field Near an Isolated Roughness Element

Figures 2(a) through 2(c) illustrate selected features of the mean flow field in the vicinity of the diamond trip with h = 0.015", as well as in the wake region downstream. The presence of the roughness element leads to a small region of flow reversal in the vicinity of the trip (Fig. 2(a)). Most of the intermediate to far wake flow is dominated by a strong streamwise streak where upwelling due to roughness induced perturbation causes the boundary layer thickness to be substantially larger in comparison to the unperturbed flow (Fig 2(c)). The centerline streak is surrounded by a pair of streamwise streaks with reduced boundary layer thickness and increased temperature gradient near the surface (Figs. 2(a) and 2(b)), presumably associated with the horseshoe vortex system that begins near the front of the trip element . The streaky structures remain prominent for large distances behind the roughness element, all the way to the trailing edge of the 16 inch model.

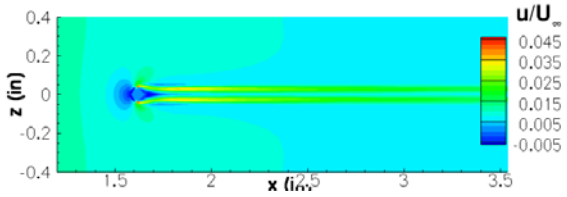

(a) Contours of *u*-velocity at *y* = 0.0002".

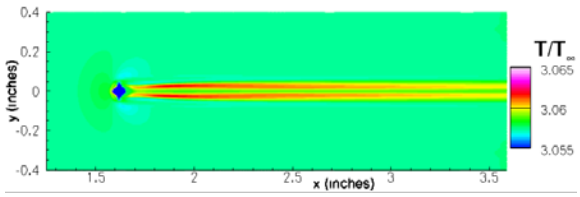

(b) Temperature contours at *y* = 0.0002".

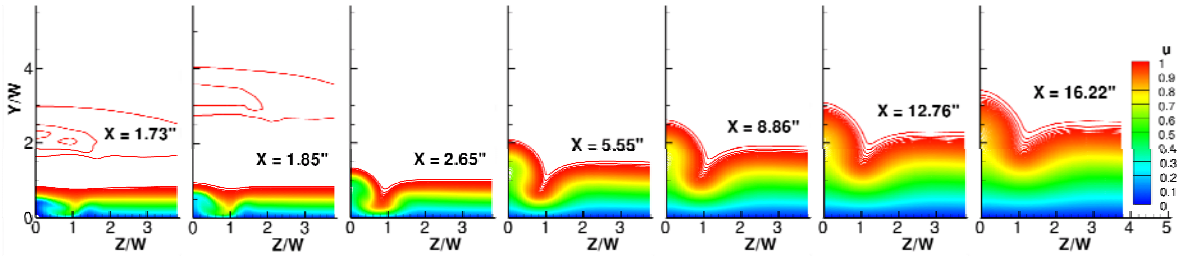

(c) Streamwise velocity contours in roughness wake. Due to spanwise symmetry of the flow field, only the right half of the wake region is shown. Both abscissa and ordinate are normalized by the frontal half width w = b cos(π/4).

Figure 2. Mean flow past a diamond trip with h = 0.015".

Unlike the wake of a spanwise periodic array of roughness elements, for which the amplitude of the stationary streaks can be easily defined in terms of either the peak or the root-mean-square variation in the streamwise velocity component, it is not obvious how to define an appropriate analogous measure for an isolated roughness element. Following Fransson et al.,[24] we define the streak amplitude A_u as one half of the maximum spanwise variation in the streamwise velocity component normalized by the free-stream velocity. The streak amplitude at h = 0.015" generally decreases with distance downstream of the

roughness element (Fig. 3(a)). Figure 3(b) displays the spanwise velocity profiles at the wall-normal height corresponding to the peak spanwise variation in the *u*-velocity component. It is seen that the peak velocity at this height remains almost constant with distance over the range of locations included in the figure. Thus, the decrease in streak amplitude A_u is primarily due to the reduction in velocity deficit associated with the low-speed streaks in the center and on the outer flanks of the high speed streaks.

The variation of the streak amplitude with the roughness height is plotted in Fig. 4. It may be observed that, at the largest roughness height (h = 0.02") considered in the figure, the streak amplitude plateaus out at large distances indicating a qualitative change in the wake structure. Indeed, velocity contours analogous to Fig. 2(c) indicate that, for h = 0.020", the mushroom shaped structure near the symmetry plane continues to lift upward due to the self-induced velocity field associated with a pair of streamwise vortices. Far enough downstream, this mushroom structure almost separates from the rest of the boundary layer flow (Fig. 5(a)). On the other hand, for small enough roughness heights (h = 0.0075" and h = 0.004" in Fig. 4), the streak amplitude decays rather rapidly immediately behind the roughness element and, hence, the streak amplitudes within the intermediate to far wake region are relatively small. The benign character of the velocity perturbations associated with the roughness wake at this height is shown in Fig. 5(b).

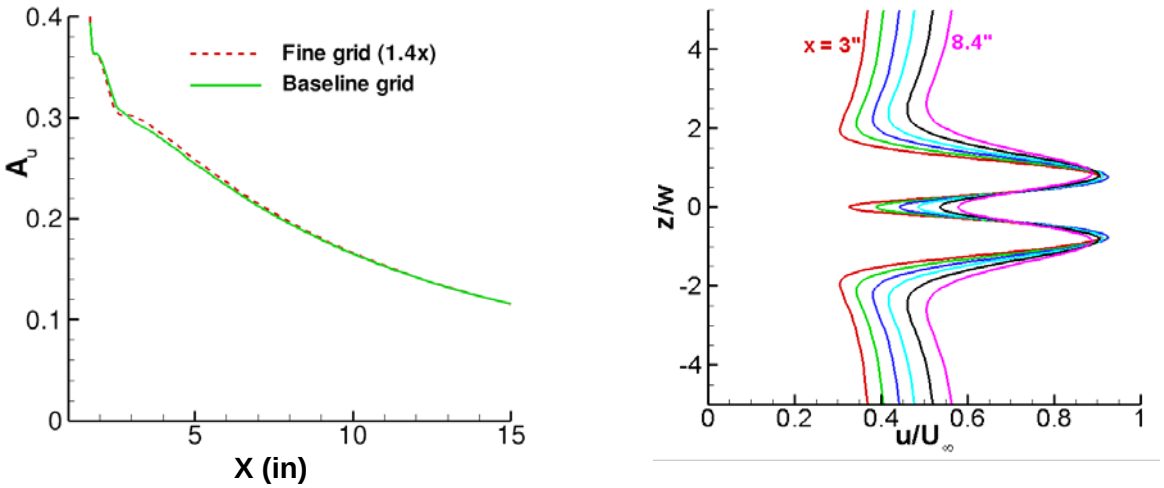

(a) Streak amplitude A_u as function of streamwise coordinate (in inches). Prediction based on the finer grid is indicated by dashed line.

(b) Spanwise profiles of u-velocity at a wall-normal height corresponding to peak spanwise variation for x = 3" to x = 8.4".

Figure 3. Streamwise evolution of streak amplitude for h = 0.015".

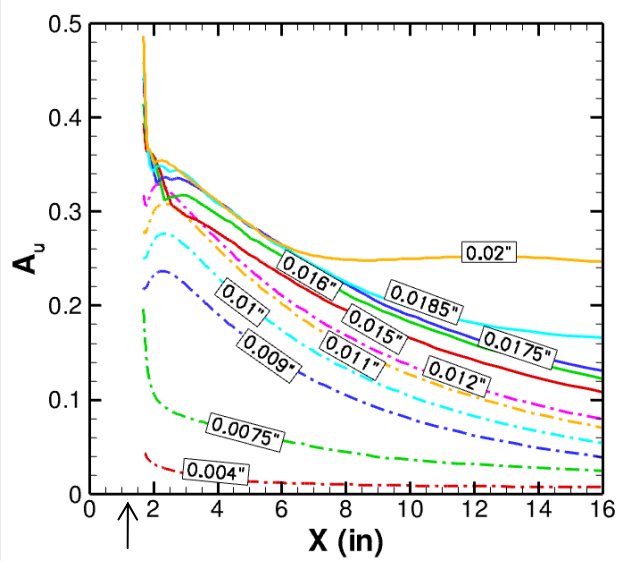

Figure 4. Amplitudes of streamwise velocity perturbation associated with roughness induced streaks. Location of roughness element is indicated by the arrow below the horizontal axis.

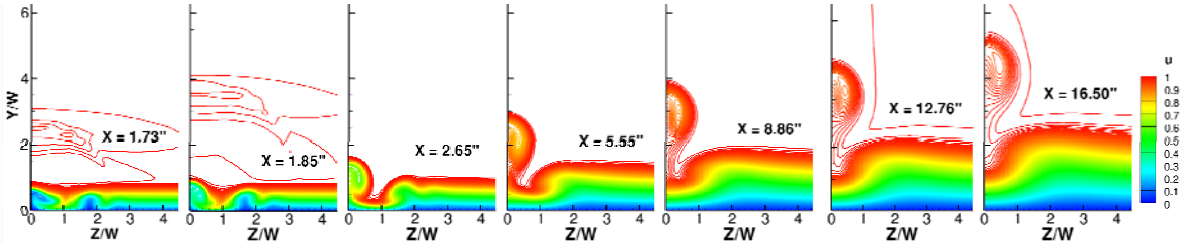

(a) h = 0.020”.

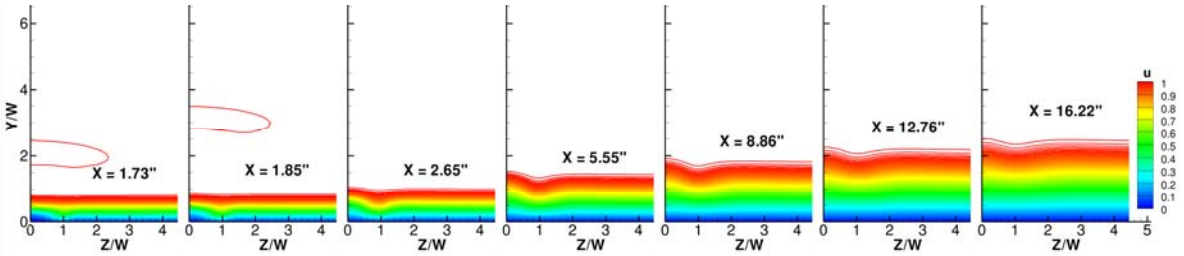

(b) h = 0.0075”.

Figure 5. Streamwise velocity contours in roughness wake. Due to spanwise symmetry of the flow field, only the right half of the wake region is shown. Both abscissa and ordinate are normalized by the frontal half width w = b cos(π/4).

B. Stability Characteristics of Wake Flow behind an Isolated Diamond Trip

The stability of the roughness wake behind the diamond trip with h = 0.015” is studied next. Before that, however, a few remarks concerning the instability characteristics of the unperturbed boundary layer flow are presented.

Since the spanwise and wall-normal length scales of the boundary layer streaks in the wake are comparable to each other, the modified boundary-layer flow has a strongly inhomogeneous character in both *y* and *z* directions. Therefore, its stability characteristics are more appropriately studied by solving a 2D eigenvalue problem,[25–27] rather than using the conventional linear stability analysis, which is based on the assumption of basic state inhomogeneity in a single spatial coordinate (viz., the surface normal direction). Instability characteristics of stationary streamwise streaks in low-speed boundary layers have been studied in Refs. 28–33. It was shown in Ref. 30 that streaks with a sufficiently large amplitude could support a rapidly growing, primarily inviscid instability mechanism but that the presence of lower amplitudes streaks reduced the growth rates of the Tollmien-Schlichting instability modes (see, also, Refs. 32 and 33 in this context).

Spatial stability of the computed streaks was examined at multiple streamwise locations in the roughness wake using the methodology described in Ref. 34. Both even (i.e., symmetric or varicose) and odd (antisymmetric or sinuous) modes of instability were examined as part of this instability analysis. The spatial growth rates of the dominant even and odd mode instabilities at x=3" are plotted in Fig. 6(a). The fluctuations associated with either mode are concentrated over the narrow spanwise extent of the streaks (Fig. 6(b)), which is significantly smaller in comparison to the spanwise wavelength of the dominant first mode instability of the unperturbed boundary layer flow. As seen from Figs. 6(b) and 6(c), velocity fluctuations associated with the even mode are concentrated near the top of the mushroom-like structure associated with secondary flow upwelling, i.e., in the region of increased wall-normal shear (*du/dy*) as seen from the top part of Fig. 6(c). In contrast, the odd modes are concentrated on either side of the mushroom structure, where the spanwise shear (*du/dz*) is large (see the bottom part of Fig. 6(c)). Qualitatively speaking, this instability structure is not too different from that observed in the context of spanwise periodic arrays of symmetric trip shapes[17] or other shapes of isolated trips[19] or, for that matter, secondary instability of finite amplitude Gortler vortices.[25–27]

Due to the challenges in making detailed, off surface measurements in high-speed boundary layers, the measurement of surface pressure fluctuations may provide a promising alternative to track the evolution of boundary layer instabilities (e.g., Ref. 35). Representative mode shapes of pressure fluctuations associated with even and odd modes of instability at x=3" are plotted in Figs. 7(a) and 7(b), respectively. The peak surface pressure fluctuations along the surface are weaker than the off-surface maxima, but only by a factor of nearly 4 in the case of the even mode and a factor of approximately 2 in the case of the odd mode. Due to the antisymmetric behavior of the odd mode, a transducer at the symmetry plane that has a sufficiently small sensing area would respond only to the even mode fluctuations.

Figure 8 presents the instantaneous contours of the streamwise velocity field synthesized from a superposition of the 3D mean flow and the spatially growing, unsteady streak instabilities of a given type, with the initial instability amplitude assigned to be 0.1% at the origin. For simplicity, the streak flow is assumed to be parallel, and the flow visualization is synthesized on the basis of the local flow and instability characteristics at x = 3". The visualizations from Figs. 8(a)-(b) confirm that the even mode of instability induces varicose motions of the underlying stationary streaks, whereas the odd mode leads to sinuous perturbations.

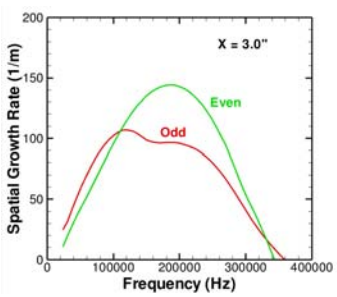

(a) Growth rates of dominant even (*y*) and odd (*z*) modes at a fixed station (*x*=3").

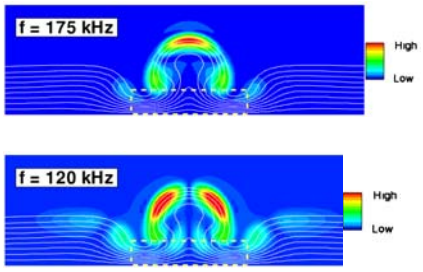

(b) Representative mode shapes of even (top figure) and odd mode (bottom figure) disturbances at x=3" (white lines indicate the associated contours of basic state *u*-velocity distribution).

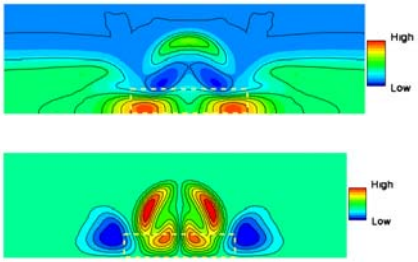

(c) Contours of basic state shear in *y* and *z* directions: *u*-velocity gradients at x = 3".

Figure 6. Instability characteristics of stationary streaks behind an isolated roughness element. (The *y*-*z* classification indicates the direction of the basic state shear that is primarily responsible for the destabilization of a given mode.)

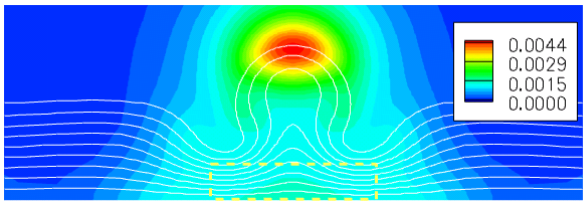

(a) Even mode (f = 175 kHz).

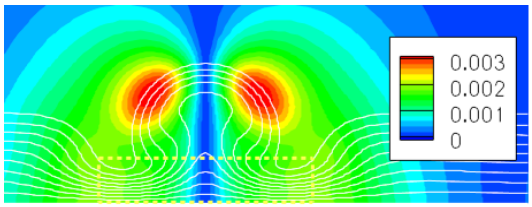

(b) Odd mode (f = 120 kHz).

Figure 7. Representative mode shapes of pressure fluctuations (nondimensionalized with respect to $\rho_\infty U_\infty^2$) due to even and odd mode disturbances (white lines indicate the associated contours of basic state *u*-velocity distribution; yellow dashed rectangle indicates the frontal view of the diamond trip). Mode shapes are normalized such that the peak temperature fluctuation (scaled by free-stream temperature) has unit magnitude.

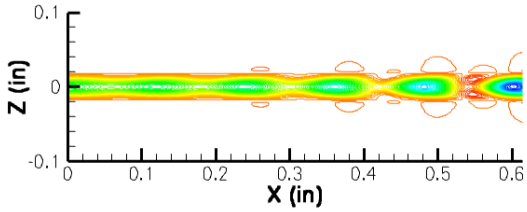

(a) Even mode 1 (f = 175 kHz).

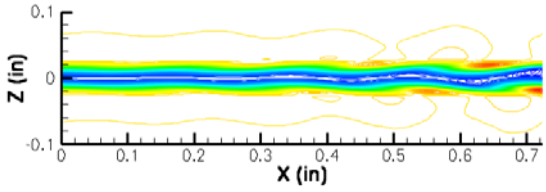

(b) Odd mode (f = 120 kHz).

Figure 8. Instantaneous *u*-velocity contours over a suitably selected constant-*y* plane for the streak flow as perturbed by even and odd instability modes in the vicinity of the x = 3".

The streamwise evolution of the symmetric and antisymmetric instability modes along the length of the plate may be determined by integrating the local amplification rates predicted via the spatial eigenvalue analysis. The cumulative amplification ratios (N-factors) of several fixed frequency disturbances spanning the frequency range of each mode type are shown in Fig. 9. Each curve denotes a specific frequency from the range of unstable frequencies corresponding to a given family of modes. Because the instability analysis begins slightly downstream of the trip, the growth of instabilities in the immediate vicinity of the trip has not been accounted for in computing the N-factors plotted in Fig. 9. The role of disturbance dynamics in the vicinity of the roughness element is addressed via direct numerical simulations in Section VI.

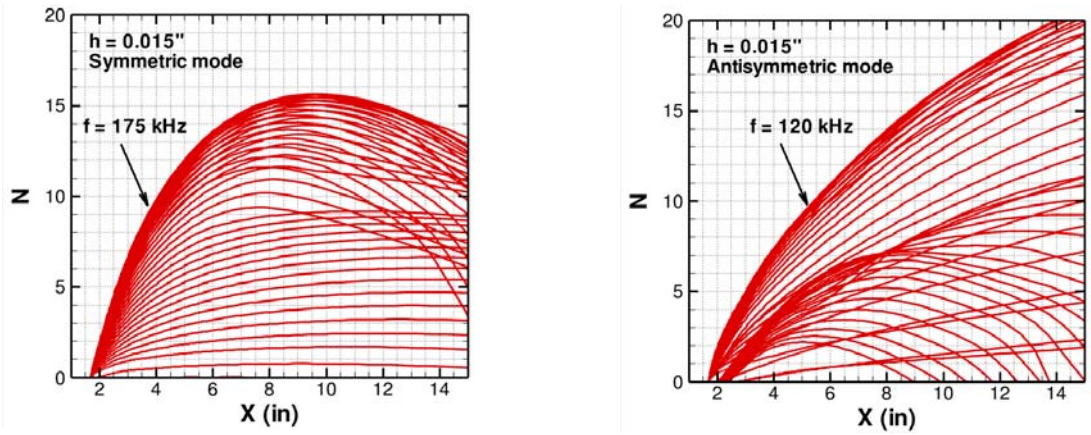

(a) Even (i.e., symmetric) modes. **(b) Odd (i.e., antisymmetric) modes.**

Figure 9. Streamwise evolution of integrated logarithmic amplification ratios (i.e., N factors) of wake instabilities for diamond trip with h = 0.015".

Figure 9 shows that both even and odd mode instabilities are dominated by a relatively small range of frequencies, with the dominant frequencies for even modes being larger than those of the odd modes. Whereas the most unstable even modes begin to decay towards the aft end of the plate, the odd modes are predicted to amplify over considerably larger distances. The peak N-factor for either mode type is significantly large, so transition is expected to occur within the length of the plate. For this diamond trip with h = 0.015", the even modes are predicted to grow somewhat faster and, hence, may dominate the transition process if the initial amplitudes of both modes are comparable. If experimental measurements confirm the role of streak instabilities during roughness induced transition, then N-factor correlations could be developed to predict the bypass transition process via physics based methodology.

IV. PARAMETER STUDY

In this section, trends related to significant roughness parameters are explored by extending the computations in Section III to include the effect of roughness height and face width of the diamond trip.

A. Effects of Trip Height on Wake Instability

N-factor evolution for selected trip heights is plotted in Fig. 10. It may be seen that, when the trip height is reduced to h = 0.01", the peak N-factors associated with both even and odd modes of instability become relatively small and, therefore, the streak instabilities may not cause transition on their own, especially if their initial amplitudes are sufficiently small (e.g., as would be the case in a benign disturbance environment). However, the N-factors are large enough at both h = 0.012" and h = 0.015" that transition onset may occur over the plate. In general, the maximum N-factors over the length of the model are associated with the odd modes. However, once the even modes become sufficiently strong

(e.g., h=0.015”), their initial growth is more rapid than that of the odd modes. Thus, if the value of the N-factor that correlates with the onset of transition is less than 9, say, then the even modes achieve that N factor earlier than the odd modes.

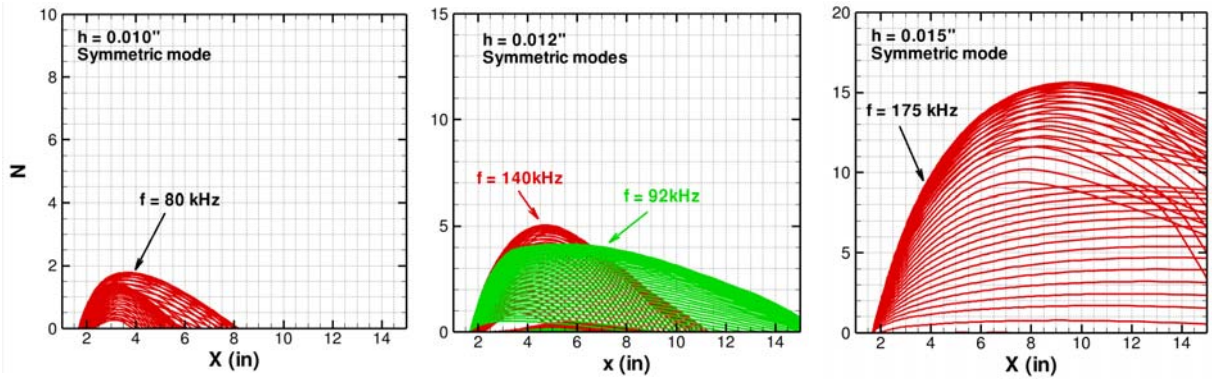

(a) Even (i.e., symmetric) modes.

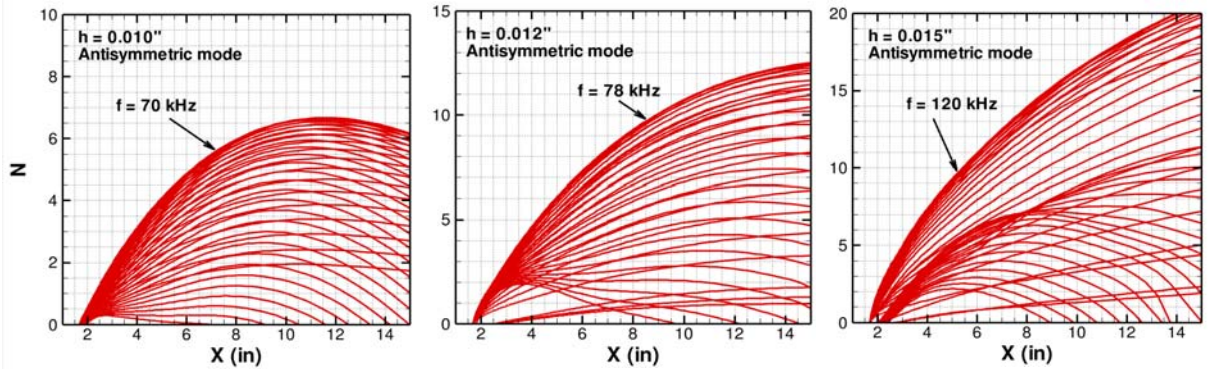

(b) Odd (i.e., antisymmetric) modes.

Figure 10. N-factor evolution at selected roughness heights.

If one assumes the transition onset to be correlated with N=9 (modeling transition in a relatively quiet disturbance environment) or N=5 (modeling transition in a noisy environment), then the predicted transition onset location can be plotted as a function of the roughness height (Fig. 11). The trend from Fig. 11 suggests that the roughness heights considered are certainly post-critical, although the asymptote for effective roughness height may not yet have been attained. Transition behavior at smaller roughness heights where the streak instabilities do not have large enough N-factors to cause transition on their own is the topic of an ongoing study and will be reported in the future.

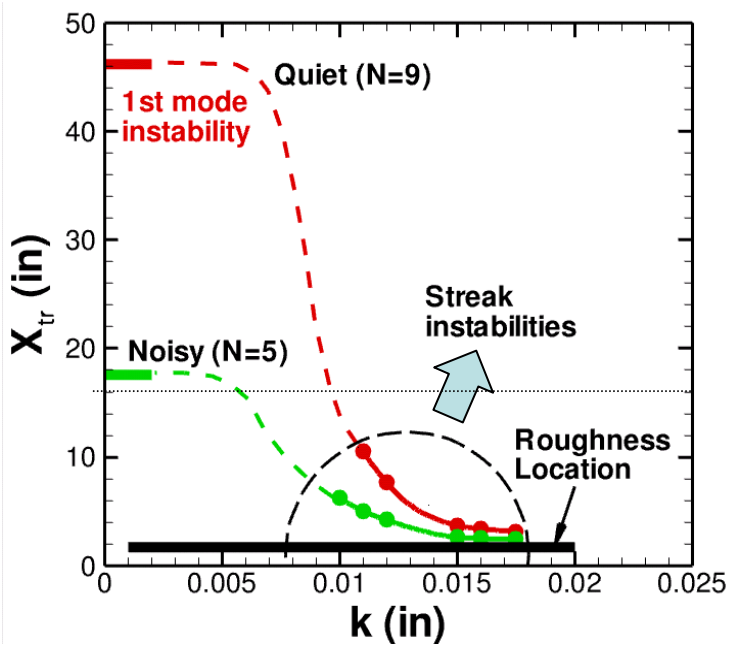

Figure 11. Variation of predicted transition onset Reynolds number with roughness height. Dashed lines indicate schematic of expected transition behavior at post-critical roughness heights. Dotted line at x_{tr} = 16" indicates the trailing edge of the flat plate model. Dashed semicircle indicates the portion of each curve that is dominated by streak instabilities.

B. Effects of Trip Aspect Ratio

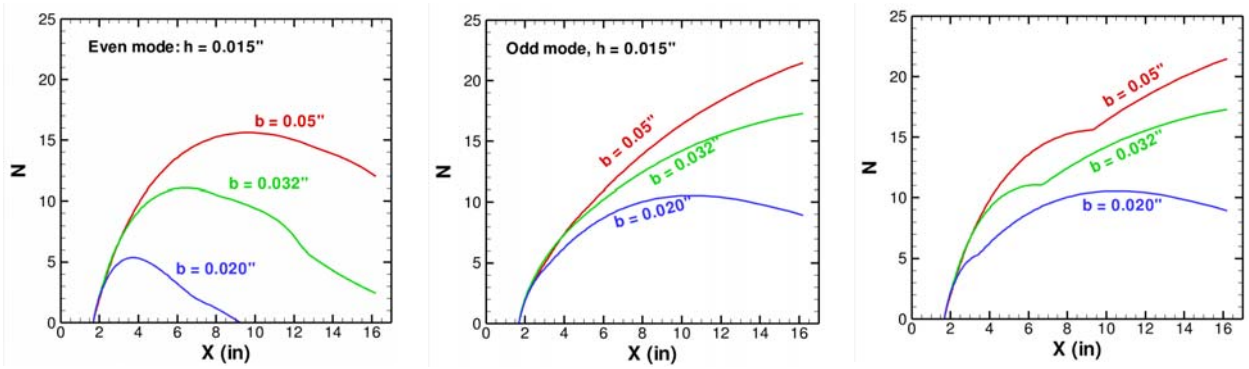

(a) Even modes of instability. **(b) Odd modes of instability.** **(c) Combined envelope.**

Figure 12. N-factor evolution for streak instabilities in trip wake as function of trip width b.

The effects of trip width b on the stability of the roughness wake are considered in Figure 12, wherein the envelopes of N-factor curves for odd and even mode disturbances are plotted for selected values of b at a fixed trip height (h = 0.015"). The combined N-factor envelope, which switches from even modes to odd modes at farther downstream locations, is shown in Fig. 12(c). The variation in transition onset Reynolds number with trip width can be estimated from Fig. 12(c) by assuming a value for the correlating N factor. For both N=9 and N=5, the change in predicted transition location from b = 0.05" to b = 0.032" is rather negligible; however, a finite downstream shift is noted when the trip width is further reduced to b = 0.02". The trend in Fig. 12(c) suggests, in fact, that a further reduction in trip width below b = 0.02" may cause the peak N-factor to drop below N=9, indicating that transition would be unlikely to occur as a result of streak instabilities alone.

C. Effects of Trip Shape

To examine the effect of trip shape on the wake flow, computations were carried out for two additional shapes, a cylindrical trip and a smoother trip shape corresponding to a spherical surface. In both cases, the peak trip height is held fixed at h = 0.015" and the radius of the circular footprint is set equal to the frontal half width w (= b cos(π/4)) of the diamond trip from sections 2 and 3. Variation of streak amplitude A_u with distance for all three trip shapes is shown in Fig. 13(a). Visualizations of the near surface flow (similar to Fig. 2(a) for the diamond trip) are shown in Fig. 13(b). Whereas the streak amplitudes for the diamond trip and cylindrical trips are comparable to each other, the spherical trip leads to lower streak amplitudes. The weaker perturbation associated with the spherical trip are also shown in Fig. 13(b), which shows a smaller region of flow reversal behind the trip and more rapidly decaying high-speed streaks in the near-wall flow. While stability computations for the spherical trip have not been carried out as yet, one would expect that the growth of instability modes will be correspondingly weaker relative to the diamond and cylindrical trips.

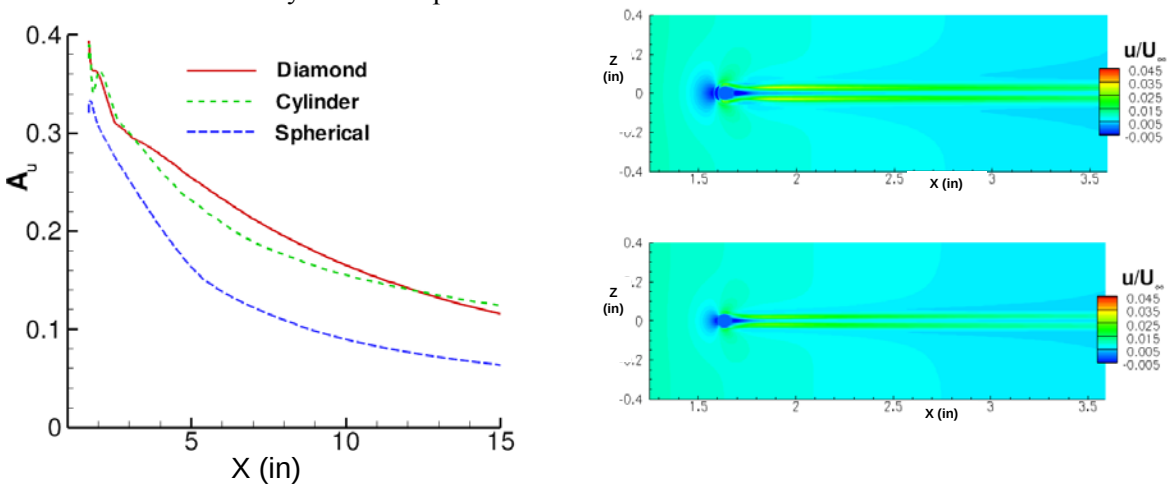

(a) Evolution of streak amplitude for different roughness shapes.

(b) Contours of *u*-velocity at *y* = 0.0002" (Top: cylindrical trip, bottom: spherical trip; corresponding plot for diamond trip is shown in Fig 2(a)).

Figure 13. Effect of trip shape on mean flow behavior at a fixed trip height of h = 0.015".

D. Effects of Multiple Roughness Elements

Naturally occurring surface nonuniformities, such as the roughness shapes induced by surface ablation, tend to be spatially distributed in nature. Thus, it is important to investigate the effects of spatial proximity between the individual roughness elements, particularly when certain elements lie within the wake of upstream elements. To study the interaction between multiple trips aligned with the flow direction in a simple context, the flow past a pair of isolated diamond trips (see Fig. 14) is examined next. The width of each trip is fixed at b = 0.05" while the streamwise spacing between the respective centers corresponds to d = 0.1575". Figure 15 compares the streak amplitudes associated with the trips in tandem with those due to a single trip with the same height. Results for the relatively small height of h = 0.004" are shown in Fig. 15(a), whereas those for h=0.01" are shown in Fig. 15(b). The streak amplitudes produced by a single trip with h = 0.004" are weak enough that no significantly strong wake instability had been noted for that case. However, the flow approaching the downstream trip has sufficiently recovered from the relatively strong nearfield disturbance due to the upstream trip, that the second trip is able to produce a comparable wake disturbance augmenting the streak amplitudes due to the upstream

trip. Thus, it is possible that, at the present combination of trip spacing and trip height, the introduction of additional trips would lead to sufficient reinforcement of the streak amplitude and, hence, strong enough wake instabilities that could potentially cause transition even at a smaller height. The augmentation of streak amplitude is consistent with the asymptotic theory by Goldstein[36] for sufficiently small roughness heights. However, it should be kept in mind that the streak amplitudes at smaller heights decay more rapidly than those at larger roughness heights (Fig. 4) and this decay would limit how small distributed roughness height can be while still producing a large enough impact on the transition process.

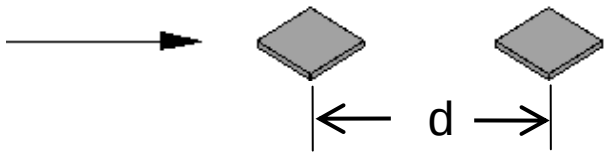

Figure 14. Schematic of a pair of trips in tandem arrangement (streamwise spacing between the centers of the two trips is given by d = 0.1575").

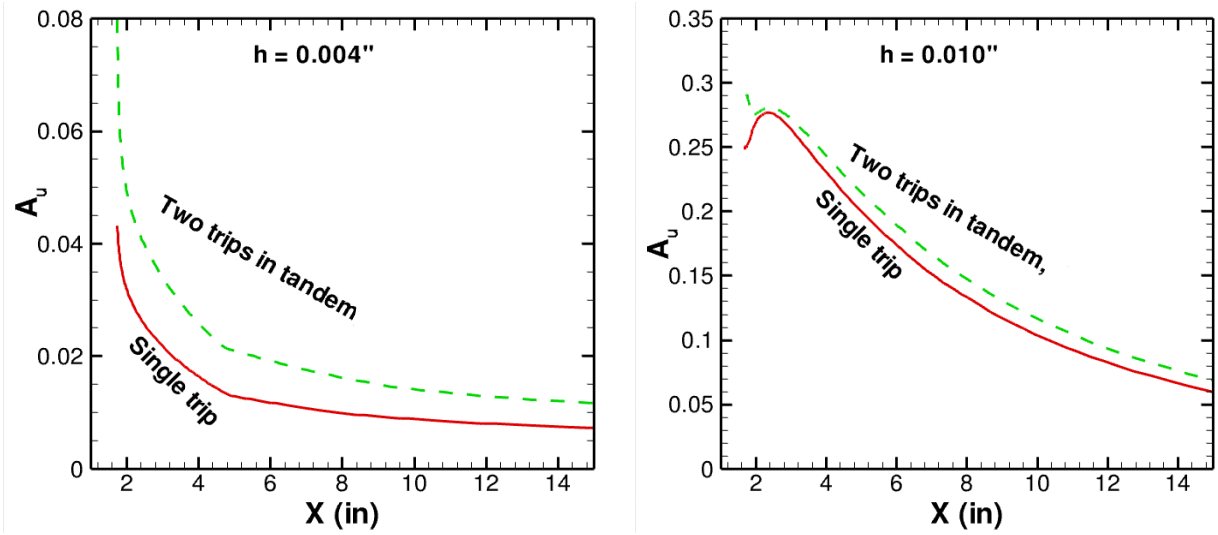

(a) Smaller trip height: h = 0.004". **(b) Larger trip height: h = 0.010".**

Figure 15. Comparison of streak amplitude evolution for a single trip and a pair of trips in tandem (streamwise spacing between the centers of the two trips is given by d = 0.1575").

The larger trip height of 0.01" leads to wake instabilities with an N-factor greater than 5 and, hence, has the potential to cause transition on its own in a noisy environment. Due to the stronger nearfield disturbance near the trip location (not shown in Fig. 15), the flow approaching the downstream trip has not recovered as much as for the h = 0.004" case. This leads to a significantly weaker augmentation of the streak amplitude as seen from Fig. 15(b) and, hence, only a small upstream shift in transition location as a result of the downstream roughness element.

V. MODELING THE EFFECTS OF SPANWISE ASYMMETRY AND CROSSFLOW

The results presented in Sections III and IV pertained to a spanwise symmetric trip in a flat plate boundary layer in the Supersonic Low Disturbance Tunnel (SLDT). Recently, in-flight transition

measurements have been carried out with space shuttle Discovery, as part of Boundary Layer Transition (BLT) Detailed Test Objective (DTO) for flights STS-119 and STS-128.[37–40] For STS-119, a specially designed tile with a 0.25" bump was installed on Discovery's bottom surface near the port main landing gear door, with the goal of obtaining transition data for a known shape of roughness element resembling a protruding gap filler. For STS-128, a 0.35" trip was used to induce transition at an earlier point during the reentry trajectory. Supporting wind tunnel measurements have been carried with a scaled version of the same trip mounted on a flat plate model which was tested in the 31 Inch Mach 10 Wind Tunnel at NASA Langley.[41] The DTO trip configuration differs from the trip configurations in Sections III and IV in two important respects, namely, the trip shape is asymmetric with respect to flow direction and, secondly, the basic flow within the region of interest includes a mild crossflow. To gain partial (and qualitative) understanding of these differences, additional computations were performed as part of the present study. The findings from those computations, which are intended to complement the insights garnered from separate computational studies[42,43] that are focused specifically on the wind tunnel configuration from Ref. 41, are summarized in this section.

A. Spanwise Asymmetric Trip Geometry

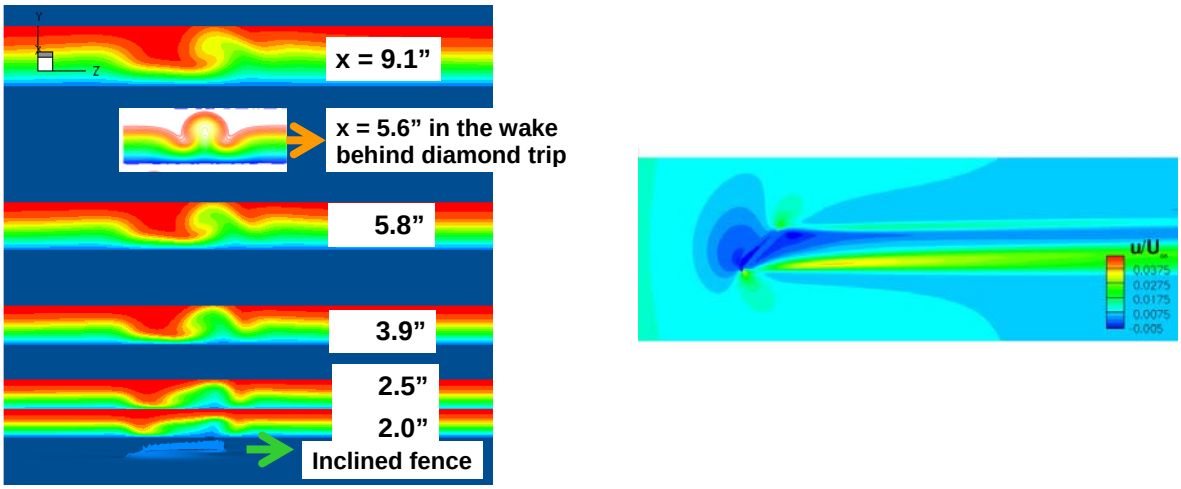

(a) Streamwise velocity contours at selected streamwise locations in roughness wake. For reference, a typical streak structure associated with a symmetric diamond trip with the same height is also shown.

(b) Wall shear distribution visualized via streamwise velocity contours at a small fixed height (y=0.0002") above the plate surface.

Figure 16. Flow past a rectangular fence inclined at 45-deg with respect to flow direction. Trip location and other flow conditions are same as the diamond trip in Fig. 2.

Effects of an asymmetric trip shape with respect to the flow direction were modeled in the context of a rectangular fence mounted at 45 degrees with respect to the x-axis. To model the large aspect ratio of the relatively wider DTO trip, the width of the fence was set equal to 9 times the trip height of h = 0.015". To allow comparison of wake structures with the diamond trip examined hitherto, the boundary layer parameters and trip location were chosen to be identical to those listed in Section II. The streamwise velocity contours at selected stations within the roughness element wake are shown in Fig. 16(a). The contours of wall-shear distribution are plotted in Fig. 16(b).

Even though the trip shape itself is symmetric, its inclination with respect to the flow direction makes the wake flow highly asymmetric as shown in Fig 16(a). The distribution of boundary layer thickness still exhibits a prominent streak corresponding to increased thickness. However, its spanwise location is

displaced relative to the center plane of the inclined fence and no longer has the mushroom-like shape observed earlier for the symmetric diamond trip. The shape of this streak now bears some resemblance to the axial velocity contours associated with a finite amplitude crossflow vortex in a three-dimensional boundary layer. Furthermore, the surrounding pair of streaks corresponding to reduced boundary layer thickness involves a prominent asymmetry in terms of both the strength (i.e., reduction in boundary layer thickness) and the spanwise extent of both constituent streaks. In particular, the streak on the $z < 0$ side (i.e., corresponding to the leading edge of the inclined fence or, equivalently, the left hand side in Fig. 16(a)) is considerably wider and deeper than its counterpart on the $z > 0$ side.

Instability analysis of the asymmetric wake flow shown in Fig. 16 has not been carried out yet. However, given the modified character of the streamwise velocity contours behind the inclined fence, one expects that the mode shapes of the streak instabilities would be significantly different from the even and odd modes of the wake behind the symmetric diamond trip. In particular, similar to the family of high-frequency secondary instabilities driven by the spanwise gradients of the basic state associated with a stationary crossflow vortex,[34] an analogous family of streak instabilities is expected to be concentrated on the right hand ($z > 0$) portion of the abovementioned streak corresponding to increased boundary layer thickness.

B. Effects of Crossflow on Spreading of Turbulence

Besides being a likely influence on the transition process behind the roughness element, three-dimensionality of the underlying boundary layer can also influence the propagation of the turbulent wedge subsequent to flow transition as well as the variation of turbulence characteristics across the width of this wedge. Wedge propagation characteristics (i.e., spreading of turbulence within the downstream flow) can have important practical implications, as it determines what parts of the vehicle structure are exposed to the increased aeroheating associated with the turbulent flow. In controlled experiments such as those involving the DTO flights, the wedge propagation characteristics also determine the placement of the limited amount of surface mounted instrumentation. Even if the angular variation in flow direction across the thickness of the boundary layer is small, the effect of this variation is cumulative and, therefore, it is important to determine whether the centerline of the wedge is primarily aligned with the inviscid streamline or the wall shear or an intermediate direction.

One way to model crossflow effects is to use Reynolds averaged Navier-Stokes (RANS) equations in conjunction with an artificial origin of turbulence within a compact region near (or just behind) the trip location. This method is particularly well-suited to examine turbulence propagation within the complex flow field over a re-entry vehicle. However, the level of physical fidelity associated with the resulting predictions is also limited by the underlying turbulence model. Therefore, the effects of boundary layer crossflow are examined using using direct numerical simulations (DNS) of a turbulent spot developing over a flat surface. It should be noted, however, that the presence of a trip introduces additional crossflow within its wake and neither of the above two methodologies account for the wake and its effect on turbulence spreading behind the trip.

Simulations are performed using a high order flow solver based on 7th order WENO scheme for the convective flux terms. The DNS code has been extensively tested for fully turbulent flows in previous work (e.g., Ref. 44). Although not shown, additional validation has also been performed in the context of the propagation of linear instability waves in a 2D, high-speed boundary layer.The baseline (i.e., zero crossflow) flow configuration corresponds to a Mach 2 flat plate boundary layer[45] with T_∞=200K and ρ_∞=0.1kg/m^3. Crossflow is introduced in the form of an artificially imposed, self-similar, jetlike velocity profile $u_{cf}(\eta) = A \exp(-c\eta^2)$, which is introduced via a suitably defined body force term. Here, η denotes the boundary layer similarity variable. The parameter c is chosen so that the maximum crossflow velocity occurs at $z/\delta_{0.995} = 0.265$ and the crossflow amplitude A is chosen to yield a -15^o inclination of the surface

shear vector with respect to the *x*-axis, i.e., the flow direction at the edge of the boundary layer. The latter crossflow inclination at the surface was deemed large enough to produce an easily discernible impact on the evolution of the turbulent spot.

The turbulent spot is induced via a localized, impulsive blowing at the surface. The resulting disturbance evolves into an arrowhead shaped turbulent spot that grows in size as it propagates downstream. Figure 17(a) shows a perspective view of the turbulent spot at a selected instant of time, both with and without the crossflow. In the absence of the any crossflow, the spot has the classic arrowhead shape with streamwise elongated structures within the so called becalmed region immediately behind the trailing edge of the spot.

To determine the trajectory of the turbulent spot, the location of the spot was estimated via visual examination of the spot using isosurface plots of the surface normal vorticity ω_y. Figure 17(b) illustrates the spot position at three selected instants of time. A definite transverse movement accompanying the streamwise advection of the spot may be noted. The center of the spot at any given instant of time is estimated as the average of the streamwise and spanwise extremities of the ω_y iso-surface. The trajectory of the spot determined in this manner is well approximated by a linear fit corresponding to an inclination of -5.6^o with respect to the inviscid flow direction along the x axis. Thus, the direction of spot propagation based on the selected metric falls in between the flow directions near the surface and the edge of the boundary layer, but is closer to the latter direction. The streamwise convection speed of the spot center is approximately $0.73U_\infty$.

Estimates of the spot trajectory based on other metrics have also been attempted and yield somewhat different propagation angles within the *x*-*z* plane. But, the overall conclusion remains the same, namely, that the spot propagates at a nonzero angle with respect to the invscid streamline.

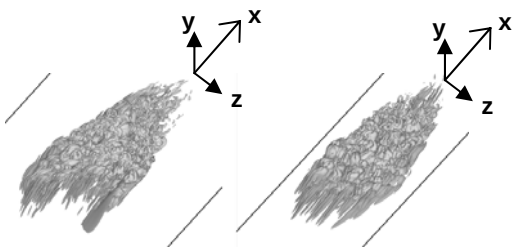

(a) Perspective view of turbulent spot with (left) and without crossflow (right). All other flow parameters identical for both cases, and the direction of crossflow is along the negative *z* axis.

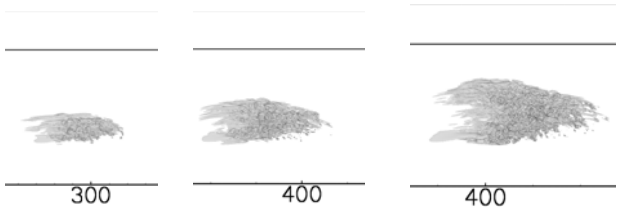

(b) Planform view of spot propagation at t = 1 x 10^{-4} sec, 1.4 x 10^{-4} sec, and 1.8 x 10^{-4} sec, respectively (from left to right). Streamwise location indicated along the horizontal axis is scaled by the boundary layer displacement thickness at the inflow (Rex = 8.2 × 10^4). The crossflow direction points upward in these figures.

Figure 17. Turbulent spot propagation in the presence of boundary layer crossflow: iso-surface of wall normal vorticity corresponding to $\omega_y\delta^*/U_\infty = \pm 0.06$.

VI. RECEPTIVITY AND NONLINEAR BREAKDOWN OF STREAK DISTURBANCES

A. Nearfield Disturbance Dynamics: Simulations of Even Mode Disturbances

Having seen that transition over a broad range of roughness sizes may be caused by instability modes of the wake flow, it is useful to examine how these instability modes may be generated in practice as well as the nonlinear mechanisms responsible for their breakdown. To that end, direct numerical simulations were performed to investigate whether the wake instability modes can be excited via roughness-induced scattering of an arbitrary disturbance field in the boundary layer flow ahead of the roughness element. The flow solver used for this DNS was the same as that used to compute the turbulent spot propagation in Section V.B. To allow high-order computations with a body-fitted grid, the original diamond geometry of the baseline trip from Section 2 was replaced with a smooth version without any sharp corners. The flow conditions were the same as the Mach 3.5 boundary from Section 2. The objective of these initial simulations was to establish the role of disturbance dynamics in the vicinity of the roughness element, which was neglected during the wake instability analysis in Sections III and IV. Hence, the choice of grid parameters was based on prior experience and no exhaustive studies were performed to quantify the numerical errors at this stage. An in-depth analysis of this and other, more refined simulations will be presented in a follow-on paper.[46]

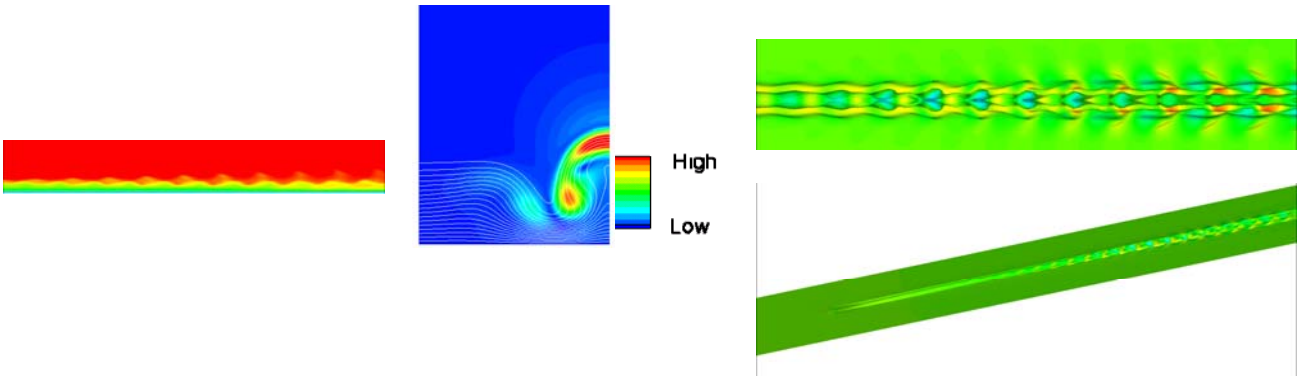

(a) Instantaneous streamwise velocity contours within roughness plane of symmetry.

(b) Root-mean-square streamwise velocity fluctuation at a representative streamwise location within roughness wake (flood contours) and contours of mean streamwise velocity (white lines) indicating streak shape. For brevity, only one half of the spanwise domain is shown.

(c) Isosurface of instantaneous streamwise velocity (u/U = 0.85): Top view and perspective view of selected regions of the flow field (contour legend same as part (b)).

Figure 18. Unsteady wake disturbances excited by 2D forcing upstream of the roughness element.

To investigate the generation of even mode instabilities, unsteadiness was introduced in the form of two-dimensional (i.e., spanwise invariant), single-frequency forcing over a localized region of the surface. The frequency of this time harmonic forcing was set equal to 200 kHz, which was predicted to fall within the frequency range of the most amplified even mode disturbances for the smooth diamond configuration. Figures 18(a) and 18(b) show the visualization of the unsteady flow field within the plane of symmetry passing through the center of the trip, and a transverse plane corresponding to constant streamwise

location, respectively. The simulations confirm the emergence of rapidly amplifying even mode instabilities within the roughness wake. At increased amplitudes, these instabilities become nonlinear and exhibit rather intricate flow structures (Fig. 18(c)).

B. Nonlinear Evolution and Transition Onset due to Odd Mode Instabilities

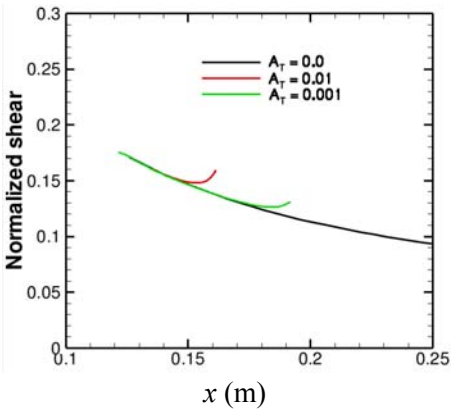

(a) Evolution of skin friction for different values of the initial amplitude A_T of the dominant odd mode disturbance with a frequency of 80 kHz.

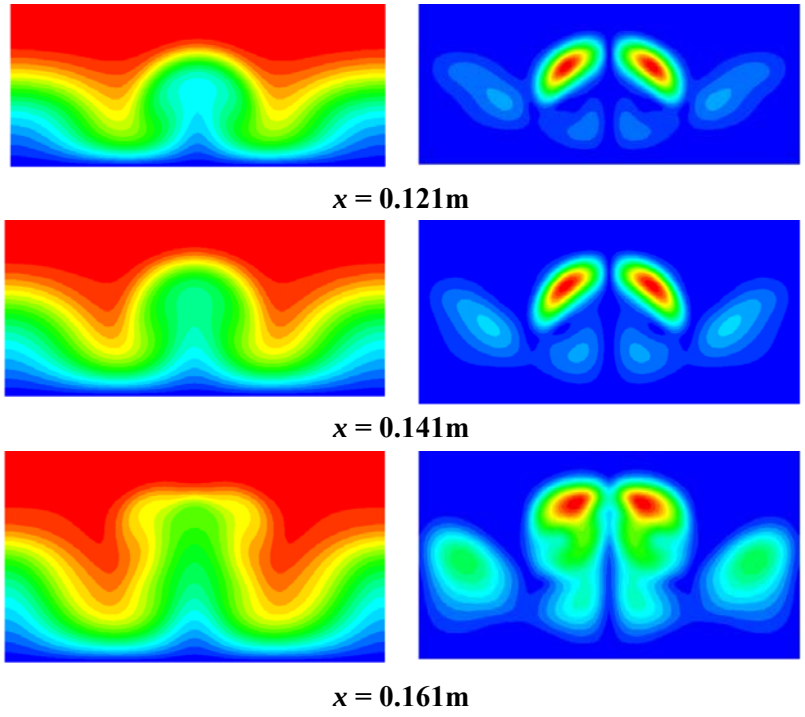

(b) Amplitude distribution of u-velocity perturbation within y-z plane at selected streamwise locations. Spanwise extent of each figure corresponds to one wavelength of the periodic trip array.

(c) Time averaged streamwise velocity distribution at selected streamwise locations.

Figure 19. Nonlinear evolution and breakdown of streaks via odd mode of wake instability behind a periodic array of diamond trips at x = 4". Array spacing corresponds to 0.1414", trip height is h = 0.02" ($Re_\theta/M_e \approx 184.5$ and $Re_\theta/M_e\ k/\delta_{0.995} \approx 88.5$).

The DNS results presented in Section VI.A indicate that the nearfield of the roughness element can scatter a fairly general incoming disturbance (including weakly unstable first mode disturbances) within the relevant band of frequencies into the mode shapes of the wake instabilities, which can then amplify and eventually lead to laminar breakdown. In light of this observation, the evolution of wake instabilities and their breakdown can be studied separately from the relatively complex but linear disturbance dynamics in the vicinity of the trip. Indeed, the former phenomena can also be studied via the parabolized stability equations (PSE). Such PSE computations were performed for a periodic array of diamond trips using initial streak profiles derived from the basic state computations with the IB methodology. The LASTRAC code developed at NASA Langley Research Center[47] was used for these computations. The downstream evolution of the stationary streaks (not shown here) was found to be in good agreement with the full Navier-Stokes computations. The PSE computations were then extended to non-stationary

disturbances corresponding to an odd mode of wake instability with a frequency of f = 80 kHz and carried through to the onset of transition as reflected by a rise in the spanwise averaged skin friction (Fig. 19(a)). The crossplane distributions of mean and fluctuating components of the streamwise velocity component at selected x-locations are shown, respectively, in parts (b) and (c) of Fig. 19.

The results in Fig. 19(a) confirm the upstream shift in transition onset location as the initial amplitude of the dominant odd mode of wake instability is increased by an order of magnitude. This shift is indicative of the likely impact of the level of free-stream disturbance environment on the bypass transition behind the trip array.

Fig. 19(b) indicates the flattening of the initially round velocity contours associated with the centerline streak as the transition process begins. This process is also accompanied by the intensification of unsteady fluctuations over a greater portion of the cross-section of the streak as seen from Fig. 19(c).

VII. SUMMARY AND CONCLUDING REMARKS

This paper presented the results of an ongoing computational study of roughness induced bypass transition in boundary-layer flows over hypersonic vehicles. Specifically, transition behind an isolated diamond trip in a Mach 3.5 flat plate boundary layer was analyzed using a combination of steady and time accurate Navier-Stokes computations, 2D partial-differential-equation based instability analysis, and parabolized stability equations. The most significant contribution of this paper is to demonstrate that, similar to the transition behind a periodic trip array in a high-speed boundary layer, the streak dominated wake flow can sustain strong high frequency, convective instabilities that can lead to early transition under conditions where the underlying boundary layer flow cannot transition via conventional linear stability mechanisms. Types of streak instability mechanisms and their relative importance as a function of trip geometry were clarified. It was shown that scattering of incoming boundary layer disturbances within the relevant range of frequencies can directly feed the wake instabilities that are responsible for transition. The nonlinear mechanisms associated with the streak breakdown process were also examined.

The analysis presented herein could pave the way for physics based predictions of roughness induced transition during atmospheric entry of hypersonic vehicles. However, before such predictions can be used in practice, it will be necessary to validate the existence of the streak instability and to confirm its role during laminar-turbulent transition via detailed measurements in a controlled laboratory experiment. Besides bridging this important gap, the upcoming experiment in the Supersonic Low Disturbance Tunnel by Kegerise et al.[11] would help delineate the limitations of the theoretical methodology presented herein and/or help improve the reliability of the predictions based on this methodology.

Acknowledgments

The work of NASA authors was performed as part of the Aerodynamics, Aerothermodynamics, and Plasma Dynamics (AAP) discipline of the Hypersonics Project of NASA's Fundamental Aeronautics Program (FAP). Development, validation, and improvements to the stability analysis code were carried out under the Supersonic Cruise Efficiency – Airframe component of the Supersonics Project. MC thanks Ms. Catherine McGinley of NASA Langley Research Center for suggesting the computational investigation of the SLDT experimental configuration. The authors would like to thank Prof. Pino Martin of Princeton University for providing the original code used to obtain the results presented in Section VI.A of this paper.

References

1. Van Driest, E. R. and McCauley, W.D., "The Effect of Controlled Three-Dimensional Roughness on Boundary-Layer Transition at Supersonic Speeds," *J. Aero. Sc.*, Vol. 27, No. 4, pp. 261-271, 1960.
2. Casper, K., Wheaton, B., Johnson, H., and Schneider, S., "Effect of Freestream Noise on Roughness-Induced Transition at Mach 6," AIAA Paper 2008-4291, 2008.
3. Morkovin, M.V., "Panel Summary on Roughness," in M.Y. Hussaini, R.G. Voight, eds, *Instability and Transition*, *Vol. I*, Springer-Verlag, pp. 265-271, 1990.

4. Morkovin, M.V., "On Roughness-Induced Transition: Facts, Views & Speculation," in M.Y. Hussaini, R.G. Voight, eds, *Instability and Transition, Vol. I*, Springer-Verlag, pp. 281-295, 1990.
5. Reda, D.C., "Review and Synthesis of Roughness-Dominated Transition Correlations for Reentry Applications," *J. Spacecraft and Rockets*, Vol. 39, No. 2, Mar.-Apr. 2002.
6. Schneider, S.P., "Effects of Roughness on Hypersonic Boundary-Layer Transition," AIAA Paper 2007-305, 2007
7. Berry, S.A. and Horvath, T.J., "Discrete Roughness Transition for Hypersonic Flight Vehicles," AIAA Paper 2007-307, 2007.
8. Berry, S.A., Auslender, A.H., Dilley, A.D., and Calleja, J.F., "Hypersonic Boundary-Layer Trip Development for Hyper-X," *J. Spacecraft and Rockets*, Vol. 38, No. 6, pp. 853-864, Nov.-Dec. 2001.
9. Reshotko, E. and Tumin, A., "Investigation of the Role of Transient Growth in Roughness-Induced Transition," AIAA Paper 2002-2850, 2002.
10. Danehy, P.M., Garcia, A.P., Borg, S., Dyakonov, A.A., Berry, S.A., (Wilkes)Inman, J.A., and Alderfer, D.W., "Fluorescence Visualization of Hypersonic Flow Past Triangular and Rectangular Boundary-Layer Trips," AIAA Paper 2007-536, 2007.
11. Kegerise, M. and King, R.A., Private Communication, 2009.
12. Berry, S.A., Chen, F.-J., Wilder, M., and Reda, D., "Boundary Layer Transition Experiments in Support of the Hypersonics Program," AIAA Paper 2007-4266, 1007.
13. Berry, S.A., Daryabeigi, K., Wurster, K., and Bittner, R.D., "Boundary-Layer Transition on X-43A," AIAA Paper 2008-3736, 2008.
14. Kimmel, R.L., Adamczak, D., Gaitonde, D., Rougeux, A., and Hayes, J.R., "HIFiRE-1 Boundary Layer Transition Experiment Design," AIAA Paper 2007-534, 2007.
15. Campbell, C.H., Garske, M., Kinder, J., and Berry, S.A., "Orbiter Entry Boundary Layer Flight Testing," AIAA Paper 2008-635, 2008.
16. Horvath, T.J., Berry, S.A., Schwarz, R., Daryabeigi, K., Splinter, S., and Ross, M., "Assessment and Mission Planning Capability for Quantitative Aerothermodynamic Flight Measurements Using Remote Imaging," AIAA Paper 2008-4022, 2008.
17. Choudhari, M., Li, F., and Edwards, J.A., "Stability Analysis of Roughness Array Wake in a High-Speed Boundary Layer," NASA FAP/HYP/AAP Quarterly Newsletter, March 2008 (also published as AIAA Paper 2009-0170).
18. Chang, C.-L. and Choudhari, M., "Hypersonic Viscous Flow over Large Roughness Elements," NASA FAP/HYP/AAP Quarterly Newsletter, March 2008 (also published as AIAA Paper 2009-0173).
19. Marxen, O., Iaccarino, G., and Shaqfeh, E.S.G., "Numerical Simulation of the Effect of a Roughness Element on High-Speed Boundary-Layer Instability," AIAA Paper 2008-4400, 2008.
20. Greene, P., "A Numerical Study of Purdue's Mach 6 Tunnel with a Roughness Element," AIAA Paper 2009-0174, 2009.
21. Colella, P. and Woodward, P.R., "The Piecewise Parabolic Method (PPM) for Gas- Dynamical Simulations," *J. Comp. Phys.*, Vol. 54, pp. 174-201, 1984.
22. Choi, J.-I., Oberoi R.C., Edwards, J.R. and Rosati, J.A., "An Immersed Boundary Method for Complex Incompressible Flows," *J. of Comp. Physics*, Vol. 224, pp. 757-784, 2007.
23. Ghosh, S., Choi, J.-I., and Edwards, J.R. "RANS and hybrid LES/RANS Simulation of the Effects of Micro Vortex Generators using Immersed Boundary Methods," AIAA Paper 2008-3728, June, 2008.
24. Fransson, J.H.M., Brandt, L., Talamelli, A., and Cossu, C., "Experimental and Theoretical Investigation of the Nonmodal Growth of Steady Streaks in a Flat Plate Boundary Layer," *Phys. Fluids*, Vol. 16, No. 10, pp. 3627-38, 2004.
25. Hall, P. and Horseman, N.J., "The Linear Inviscid Secondary Instability of Longitudinal Vortex Structures in Boundary Layers," *J. Fluid Mech*., Vol. 232, 357-375.
26. Yu, X. and Liu, J.T.C., "On the Mechanism of Sinuous and Varicose Modes in Three-Dimensional Viscous Secondary Instability of Nonlinear Gortler Rolls," *Phys. Fluids*, Vol. 6, pp. 736-750, 1994.
27. Li, F. and Malik, M.R., "Fundamental and Subharmonic Secondary Instability of Gortler Vortices," *J. Fluid Mech*., Vol. 297, pp. 77-100, 1995.
28. Brandt, L. and Henningson, D.S., "Transition of Streamwise Streaks in Zero-Pressure-Gradient Boundary Layers," *J. Fluid Mech*., Vol. 472, pp. 229-261, 2002.
29. Goldstein, M.E. and Wundrow, D.W., "Interaction of Oblique Instability Waves with Weak Streamwise Vortices," *J. Fluid Mech*., Vol. 284, p. 277-307, 1995.
30. Cossu, C. and Brandt, L., "Stabilization of Tollmien-Schlichting Waves by Finite Amplitude Optimal Streaks in the Blasius Boundary Layer," *Phys. Fluids*, Vol. 14, L57-L60, 2002.
31. Wu, X. and Luo, J., "Linear and Nonlinear Instabilities of a Blasius Boundary Layer Perturbed by Streamwise Vortices. Part 1. Steady Streaks," *J. Fluid Mech*., Vol. 483, pp. 225-248, 2003.
32. Fransson, J.H.M., Brandt, L., Talamelli, A., and Cossu, C., "Experimental Study of the Stabilization of Tollmien-Schlichting Waves by Finite Amplitude Streaks," *Proceedings of IUTAM Symposium on Laminar-Turbulent Transition*, Bangalore, India, Dec. 13-17, 2004.
33. Choudhari, M. and Fischer, P., "Roughness-Induced Transient Growth," AIAA Paper 2005-4765, 2005.
34. Li, F. and Choudhari, M., "Spatially Developing Secondary Instabilities and Attachment Line Instability in Supersonic Boundary Layers," AIAA Paper 2008-590, 2008.

35. Wheaton, B. and Schneider, S., "Roughness-Induced Instability in a Laminar Boundary Layer at Mach 6," AIAA Paper 2010-1574, Jan. 2010.
36. Goldstein, M.E., Sescu, A., Duck, P.W., and Choudhari, M., "The Long Range Persistence of Wakes behind a Row of Roughness Elements," *J. Fluid Mech.*, 2010 (In Press).
37. http://www.nasaspaceflight.com/2009/05/sts-119-blt-test-success-gains-greater-understanding-reentry/, Nov. 2009.
38. http://www.nasaspaceflight.com/2009/06/discovery-handed-special-heatshield-coating-dto-on-behalf-of-orion/, Nov. 2009.
39. Anderson, B., "BLT Flight Experiment Overview and In- Situ Measurements ," AIAA Paper 2010-0240, Jan. 2010.
40. Horvath, T., Tomek, D., Splinter, A., Zalameda, J., Krasa, P., Schwartz, R., Gibson, D., and Tietjen, A., "The HYTHIRM Project: Flight Thermography of the Space Shuttle During Hypersonic Re- Entry," AIAA Paper 2010-0241, Jan. 2010.
41. Danehy, P., Ivey, C., Bathel, B., Inman, J., Jones, S., Jiang, N., Webster, M., Lempert, W., Miller, J., and Mayer, T., "Orbiter BLT Flight Experiment Wind Tunnel Simulations: Nearfield Flowfield Imaging and Surface Thermography," AIAA Paper 2010-1571, 2010.
42. Chang, C., Choudhari, M., and Li, F., "Numerical Computations of Hypersonic Boundary- Layer over Surface Irregularities," AIAA Paper 2010-1572, 2010.
43. Yoon, S. and Barnhardt, M., "Simulations of High- Speed Flow Over an Isolated Roughness," AIAA Paper 2010-1573, 2010.
44. Martin, M. P., Taylor, E. M., Wu, M., and Weirs, V. G., "A Bandwidth-optimized WENO Scheme for the Effective Direct Numerical Simulation of Compressible Turbulence," *J. Comp. Physics*, Vol. 220, pp. 270-289, 2006.
45. Krishnan, L. and Sandham, N. D., "Effect of Mach number on the structure of turbulent spots," *J. of Fluid Mech.*, Vol. 556, pp. 225-234, 2006.
46. Choudhari, M., Li, F., Wu, M., Chang, C.-L., and Edwards, J.A., "On Roughness Induced Transition in Supersonic and Hypersonic Boundary Layers," Submitted to 30th AIAA Fluid Mechanics Conference, Chicago, June 2010.
47. Chang, C.-L., "The Langley Stability and Transition Analysis Codes (LASTRAC: LST, Linear and Nonlinear PSE for 2D, Aximsymetric, and Infinite Swept Wing Boundary Layers," AIAA Paper 2003-0974, 2003.